Preferred modes of variability and their relationship with climate change

Seok-Woo Son and Sukyoung Lee

Department of Meteorology, The Pennsylvania State University

University Park, PA 16802

July, 2005 (Revised)

Corresponding address: Seok-Woo Son, Department of Meteorology, 503 Walker Building, The Pennsylvania State University, University Park, PA 16802.

Abstract

Spatial structure of annular modes shows a remarkable resemblance to that of the recent trend in the observed circulation (Thompson et al.). This study performs a series of multi-level primitive equation model simulations to examine the extent to which the annular mode is capable of predicting changes in the zonal-mean flow response to external heat perturbations. Each of these simulations represents a statistically steady state, and differs from each other in the values of the imposed localized tropical heating ($\mathcal{H}$) and high-latitude cooling ($\mathcal{C}$).

Defining the annular mode as the first empirical orthogonal function (EOF1) of zonal-mean tropospheric zonal wind, it is found that the 'climate predictability' is generally high in the small $\mathcal{C}$ - large $\mathcal{H}$ region of the parameter space, but is markedly low in the large $\mathcal{C}$ - small $\mathcal{H}$ region. In the former region, EOF1 represents meridional meandering of the mid-latitude jet, while in the latter region, EOF1 and EOF2 combine to represent coherent poleward propagation of zonal-mean flow anomalies. It is also found that the climate predictability tends to be higher with respect to changes in $\mathcal{C}$, than to changes in $\mathcal{H}$. The implications of these findings for the Southern Hemisphere climate predictability are also presented.

1 Introduction

It has been shown that the linear trend in the zonal-mean zonal wind and temperature from the late 1960s through the 1990s is remarkably similar to the positive phase of what has become known as the annular mode[1] (Thompson and Wallace 1998; Thompson et al. 2000). A similar result was also found in global warming experiments (Fyfe et al. 1999; Kushner et al. 2001). These studies suggest that the leading empirical orthogonal function (EOF1) of a statistically stationary climate may be used to make climate predictions.

In a series of stratospheric 'degradation' experiments, however, Taguchi (2003) finds that EOF1 is not always a good predictor for the model's climate response. In his experiments, stratospheric wave breaking was turned off by making the radiative relaxation time scale in the stratosphere very short. Comparing realistic runs to the degradation runs, he found that the response of the mid-troposphere to the reduced stratospheric wave breaking has almost the same structure as the EOF1 of the realistic runs when topographic heights are either 0- or 1000-m. When the topographic height is set equal to 500 m, its response is no longer recovered by the EOF1. These results raise the possibility that the performance of EOF1 as a climate predictor may depend on the climate regime of the circulation of interest.

The goal of this study is therefore to investigate to what degree and under what conditions the annular mode, or the EOF1, is able to predict *pattern* of the zonal-mean climate change. It is important to emphasize at the outset that this study does not explore any theory

[1]Thompson and Wallace (1998) showed that the horizontal structure of the leading empirical orthogonal function of sea level pressure is to a large degree zonally symmetric, and that the associated zonal-mean meteorological fields are quasi-barotropic. This zonally symmetric, quasi-barotropic variability of the atmospheric circulation is known as the annular mode.

for predicting the sign and amplitude of $\delta\overline{[u]}$, but is only concerned with changes in the meridional structure. As such, the terms 'predictability' or 'predict' in this study follow this narrow definition. As a tool for this investigation, we use a set of idealized model runs described in Son and Lee (2005, hereafter SL). The set of model runs spans a finite parameter space where the parameters are tropical heating and high-latitude cooling. As discussed in SL, the extra heating is designed to control the intensity of the subtropical jet, and the extra cooling is adopted to control the width of extratropical baroclinic zone. The equations describing the form of the tropical heating and high-latitude cooling are given in appendix which also provides a brief summary of the numerical model used in this study. As described in the appendix, since only amplitudes of the heating and cooling are varied in the experiments, each experiment can be identified by the surface values of the heating at the equator and cooling at the poles. They are denoted by $\mathcal{H}$ and $\mathcal{C}$, respectively.

In accordance with the above goal, our strategy is to first calculate the leading EOFs of the zonal-mean zonal wind, $[u]$, for each model run, and then to compare EOF1 with the changes in the time-mean zonal-mean zonal wind, $\delta\overline{[u]}$, which result from changes in $\mathcal{C}$ or $\mathcal{H}$. Here, $\delta\overline{[u]}$ is defined as the difference in $\overline{[u]}$ between two adjacent data points in the $\mathcal{C}-\mathcal{H}$ parameter space. This difference between $\overline{[u]}$ values is calculated both for changes in the high-latitude cooling ($\delta\overline{[u]}_{\mathcal{C}}$) and for changes in the tropical heating ($\delta\overline{[u]}_{\mathcal{H}}$). The similarity between $\delta\overline{[u]}$ and EOF1 is then measured in two different ways. One is a global pattern correlation, and the other is the difference in the latitude of the local extrema in $\delta\overline{[u]}$ and in EOF1.

This paper is organized as follows. The analysis procedures are briefly described in the next section. Section 3 presents an overview of the mean flow and the behavior of the leading

EOFs in the $\mathcal{C} - \mathcal{H}$ parameter space. As will be shown, the characteristics of the EOFs are highly dependent on the mean flow structure. Furthermore, as will be shown, the predictability of changes in the zonal-mean circulation is significantly affected by the characteristics of EOFs themselves. The latter finding is described in section 4. Section 5 provides a summary and discussion. Lastly, the implications of this study for the atmosphere, focusing on the Southern Hemisphere, are presented in section 6.

2 Model analysis

For all model runs, the statistics presented in this study are derived from the last 4500 days of each 5000-day integration. Additional 10000-day simulations for the selected cases confirm that the statistics with 4500 days are sufficient. This contrasts SL who used the last 500-model days from each 800-day integration. Again, see the appendix for a brief description of the model. Figure 1a reproduces Fig. 4 of SL which summarizes the structure of the westerly jets as a function of $\mathcal{C}$ and $\mathcal{H}$. There is virtually no difference in $\overline{[u]}$ statistics between the two figures[2]. The longer integration, however, is necessary in this study to attain reliable statistics for the EOFs.

The EOFs are calculated from a covariance matrix of $cos^{1/2}\varphi \cdot [u]$ where φ is the latitude. No filtering is applied to $[u]$ unless stated otherwise. Since the sign of the EOFs is arbitrary, in order to facilitate comparisons among the simulations, the phase of the EOFs to be

[2]The boundaries of jet regimes are slightly different in the two figures. For instance, the intermediate jet at ($\mathcal{C}$, $\mathcal{H}$) = (1.00, 0.33) in Fig. 1a was defined as a double-jet state in Fig. 4 of SL.

displayed is chosen so that poleward-most peak of the EOFs has a negative sign[3]. In addition, all EOFs are presented in unit of ms^{-1} by regressing $[u]'$ ($=[u]-\overline{[u]}$) on the principal component (PC) time series. As expected from the symmetric thermal driving across the equator (see Fig. A1), the corresponding EOFs in two Hemispheres are almost indistinguishable. Furthermore, the percentage of variance explained by corresponding EOFs [denoted as Var (EOF_n) hereafter where n denotes the rank] in both hemispheres is quite similar to each other, differing by about 4% of the total fractional variance. These similarities in EOF statistics between the two hemispheres indicate that the 4500-day integration provides a reliable statistics for the purpose of this study. The EOFs to be shown below are obtained by averaging the two corresponding EOFs from either hemisphere. Likewise, $\overline{[u]}$ and $\delta\overline{[u]}$ are also calculated using model output from both hemispheres.

3 Characteristics of leading EOFs: two classes of $[u]'$ variability

Prior to comparing EOF1 with $\delta\overline{[u]}$, it is useful to examine the leading EOFs. As will be demonstrated, the characteristics of the EOFs are highly dependent on the mean flow structure.

Figure 1a summarizes the structure of the westerly jet with three categories. Following SL, a single-jet refers to a state for which both the 250- and 550-hPa $\overline{[u]}$ have a single

[3]Note that the polarity chosen in this study is reversed from the convention used in previous annular mode studies (e.g., Thompson et al. 1998). Since we are only concerned with the pattern in our analysis, this particular choice of polarity is inconsequential for the conclusion of this study.

maxima, and a double-jet refers to a state for which the 250-hPa $\overline{[u]}$ has distinct double local maxima. If neither of the above two conditions are satisfied, the state is referred to as an intermediate jet. As described in SL, a double-jet state is preferred for large $\mathcal{C}$ and small $\mathcal{H}$, whereas a single-jet state is favored if $\mathcal{H}$ exceeds a certain threshold value ($\approx$ 1.00 Kday^{-1}), regardless of the value of $\mathcal{C}$.

An examination of the temporal evolution of the 250-hPa $[u]'$ indicates that there are two classes of $[u]'$ fluctuations. One is characterized by poleward propagation from the deep tropics to high-latitudes, and the other is a meridional meander about the time-mean jet axis which is known as the zonal index. Both the poleward propagation and the zonal index/ jet meander have been found in both observations and numerical models (Riehl et al. 1950; James et al. 1994; Weickmann et al. 1997; and Feldstein 1998; for the poleward propagation; Namias 1947; Rogers and van Loon 1982; Kidson 1988; Robinson 1991; Feldstein and Lee 1998; and Hartmann and Lo 1998; for the zonal index).

Figures 2a-c show examples of the poleward propagation in terms of a one-point lag correlation map of 250-hPa $[u]'$ where the base latitude is 30°[4]. These three cases correspond to ($\mathcal{C}$, $\mathcal{H}$) = (1.00, 0.00), (0.83, 0.33), and (0.67, 0.67), and are located in the lower right corner along the slanting axis 'E' in Fig. 1a. Also shown in each panel are 250-hPa $\overline{[u]}$, the two leading EOFs, and the fractional variances, Var (EOF1) and Var (EOF2). For these three runs, where the poleward propagation appears to be the most prominent form of the zonal flow variability, the value of Var (EOF2) is comparable to that of Var (EOF1).

[4]Because of the arbitrariness of the base latitude, the same one-point correlation maps were constructed by varying the base latitude from 20° to 40°. We found qualitatively similar results, ensuring that the correlation maps shown in Fig. 2 are robust.

Figure 3a shows time series of normalized PC1 and PC2 for the case shown in Fig. 2b. For the purpose of illustration, a 10-day low-pass filter is applied to both PC time series. It is apparent that the two PCs are quasi-periodic, and are 90° out of phase. The lag-correlations between the two PCs (right panel in Fig. 3a) show that PC2 leads PC1 with a time scale of about 48 days, implying that the period of the poleward propagation is about 192 days (see also Fig. 2b).

For the other class of $[u]'$ variability, the zonal index/ jet meander, Var (EOF1) is often much greater than Var (EOF2), and the corresponding PCs are always uncorrelated. Two examples of zonal index are illustrated in Figs. 2f and 2g. These two cases correspond to $(\mathcal{C},\ \mathcal{H}) = (0.17,\ 1.67)$ and $(0.00,\ 2.00)$, and are located in the upper left corner along the axis 'E' in Fig. 1a. Unlike for the poleward propagation cases, the latitudinal distribution of correlation coefficients is almost invariant in time. Since EOF1 (EOF2) corresponds to the meandering (pulsation) of the jet (see the right side of each panel), the fact that Var (EOF1) is much greater than Var (EOF2) implies that the temporal variability is dominated by jet meander. Figure 3b shows the time series of the normalized PC1 and PC2 for the case shown in Fig. 2f. The two leading PCs show no periodicity, and are virtually uncorrelated with each other.

The above analysis suggests that the characteristics of $[u]'$ variability can be quantified by two measures in the EOF statistics. One is the ratio of Var (EOF2) to Var (EOF1). The other is the maximum lag-correlation coefficient between PC1 and PC2. We denote this ratio and the correlation coefficient by γ and χ, respectively. If $[u]'$ is dominated by the poleward propagation, both the ratio γ and the correlation coefficient χ are expected to be relatively high. Likewise, values of these two will be relatively low for the zonal index/ jet

meander case.

As can be seen from Figs. 1b and 1c, with the exception of a secondary local minima in γ, relatively small values in both γ and χ take place in the strong single-jet regime. In contrast, large values are found in the double-jet regime. These results indicate that the zonal index dominates in a flow regime with a narrow extratropical baroclinic zone (small $\mathcal{C}$) and strong tropical thermal driving (large $\mathcal{H}$), whereas the poleward propagation preferentially occurs in the regime with a broad extratropical baroclinic zone (large $\mathcal{C}$) and weak tropical thermal driving (small $\mathcal{H}$).

The secondary minima in γ (Fig. 1b), which is not found in χ (Fig. 1c), arises from a special form of zonal flow variability that occurs along the regime boundary. Figure 4 shows 250-hPa $[u]$ for the positive (solid) and negative (dashed line) phases of EOF1 along the axis 'E' of Fig. 1a. These $[u]$ fields are calculated by adding and subtracting EOF1 to the time-mean $[u]$. Unlike for all other runs, it is seen for the run with local minimum in γ (Fig. 4c) that EOF1 represents a merging and separation of the two jets. Similar behavior was noted in the two-layer model calculations of Lee and Feldstein (1996). As one moves slightly away from this local minima in γ toward upper left corner in the parameter space, the $[u]'$ variability has characteristics of both poleward propagation and zonal index until it is dominated by zonal index (see Figs. 2d and 2e). We define this parametric regime as a transition zone.

The above findings for the EOFs are summarized in Fig. 1d which shows the two classes of $[u]'$ variability with rather broad transition zone. As will be described in the following section, these three regimes of $[u]'$ variability are profoundly linked to the predictability of $\delta\overline{[u]}$.

4 Predictability of $\delta\overline{[u]}$ by EOF1

With the above information on the EOFs in hand, we now turn to the main goal of this study and examine EOF1 and $\delta\overline{[u]}$. For each data point in the $\mathcal{C}-\mathcal{H}$ parameter space in Fig. 1, we compare the EOF1 and $\delta\overline{[u]}$ of the corresponding model run. The quantity $\delta\overline{[u]}$ is defined with a forward finite differences as follows;

$$\delta\overline{[u]}_{\mathcal{C}}(\mathcal{C},\mathcal{H}) = \overline{[u]}\,(\mathcal{C}+\delta\mathcal{C},\ \mathcal{H}) - \overline{[u]}\,(\mathcal{C},\mathcal{H}).$$

and

$$\delta\overline{[u]}_{\mathcal{H}}(\mathcal{C},\mathcal{H}) = \overline{[u]}\,(\mathcal{C},\ \mathcal{H}+\delta\mathcal{H}) - \overline{[u]}\,(\mathcal{C},\mathcal{H}),$$

These two expressions of $\delta\overline{[u]}$ correspond to changes in $\overline{[u]}$ that are parallel to the $\mathcal{C}$ and $\mathcal{H}$ axes, respectively, in Fig. 1, where $\delta\mathcal{C}$ and $\delta\mathcal{H}$ are the distances in between adjacent data points in the $\mathcal{C}-\mathcal{H}$ parameter space. For example, taking the $(\mathcal{C},\ \mathcal{H}) = (0.00,\ 0.00)$ as a reference state, $\delta\overline{[u]}_{\mathcal{C}}(0.00, 0.00)$ and $\delta\overline{[u]}_{\mathcal{H}}(0.00, 0.00)$ are obtained as below:

$$\delta\overline{[u]}_{\mathcal{C}}(0.00, 0.00) = \overline{[u]}\,(0.17, 0.00) - \overline{[u]}\,(0.00, 0.00).$$

and

$$\delta\overline{[u]}_{\mathcal{H}}(0.00, 0.00) = \overline{[u]}\,(0.00, 0.33) - \overline{[u]}\,(0.00, 0.00),$$

The top panels of Figs. 5a and 5b exhibit the 250-hPa $\delta\overline{[u]}_{\mathcal{C}}$ and EOF1 along the lines 'A' and 'B' in Fig. 1a, respectively (see Fig. 4 of SL for the latitudinal profiles of 250-hPa $\overline{[u]}$). Similarly, the 250-hPa $\delta\overline{[u]}_{\mathcal{H}}$ and EOF1 along the lines 'C' and 'D' in Fig. 1a are presented in Figs. 5c and 5d. Although there are exceptions, the overall structure of EOF1 is quite similar to that of $\delta\overline{[u]}$.

In Fig. 6, the structure of EOF1 and $\delta\overline{[u]}$ are quantitatively compared with pattern correlations. Here, data from 950- to 150-hPa and from 10° to 80° are used. As expected from Figs. 5a and 5b, the correlations between the $\delta\overline{[u]}_{\mathcal{C}}$ and EOF1 are reasonably good except in the lower right corner of the parameter space (Fig. 6a). Referring back to Fig. 1d, this implies that predictability of $\delta\overline{[u]}_{\mathcal{C}}$ is relatively poor when the reference state lies in the poleward propagation regime. A similar comparison is carried out for $\delta\overline{[u]}_{\mathcal{H}}$. Unlike for $\delta\overline{[u]}_{\mathcal{C}}$, the correlations are relatively low not only in the poleward propagation regime but also in part of the zonal index regime (Fig. 6b).

The global measure described above does not discriminate the predictability of $\delta\overline{[u]}$ in the extratropics from that in the tropics/subtropics. Thus, a more detailed comparison is made by measuring the latitudinal distances between extrema in EOF1 and the corresponding extrema in $\delta\overline{[u]}$. Since the latitudinal resolution of the model (2.3°) is too coarse for this measure, a cubic-spline interpolation is applied to model output to produce 1.0°-interval data. The EOF analysis is then performed with the interpolated data. The resulting EOFs and $\delta\overline{[u]}$ structures are almost identical to those from the raw output. The bottom panels of Fig. 5 display some examples of the latitudinal location of extrema in $\delta\overline{[u]}$ (open) and EOF1 (filled squares). The latitudinal distances of these two quantities, denoted as $\delta\varphi$, in both the low- and mid-latitudes are also illustrated in Fig. 5b.

The values of $\delta\varphi$ in the parameter space are exhibited in Fig. 7. It can be seen that the maximum values of both the low- and mid-latitude $|\delta\varphi_{\mathcal{C}}|$ take place in the lower right corner of the parameter space (Figs. 7a and 7b). These are consistent with the global measure shown in Fig. 6a. As for $|\delta\varphi_{\mathcal{C}}|$, the maximum value of low-latitude $|\delta\varphi_{\mathcal{H}}|$ also occurs in the poleward propagation regime (Fig. 7c). However, the mid-latitude $|\delta\varphi_{\mathcal{H}}|$ is an exception.

The maximum value takes place in the zonal index regime (Fig. 7d), indicating that the relatively low correlation found in the jet meander regime in Fig. 6b arises mostly from the discrepancy in mid-latitudes.

It is noteworthy that $|\delta\varphi|$ exhibits a pattern similar to γ (compare Figs. 7a-c to Fig. 1b). With the exception of Fig. 7d, the region where $|\delta\varphi| \geq 2^\circ$ (unshaded area in Fig. 7) largely coincides with the region where $\gamma \geq 0.5$ (shaded area in Fig. 1b). This result suggests the rule of thumb that EOF1 is a reliable first-order indicator if $\gamma \leq 0.5$.

5 Summary and discussion

Zonal wind data from the set of idealized model simulations described by Son and Lee (2005) is used as a tool for comparing the structure of the annular mode with changes in the zonal-mean flow response to external heat perturbations, $\mathcal{C}$ and $\mathcal{H}$. Having defined the annular mode as the first empirical orthogonal function (EOF1) of the zonal-mean zonal wind ($[u]$), the comparison is made between EOF1 of a given simulation, and $\delta\overline{[u]}$. Climates for which these two quantities are more similar *in structure* are regarded as having greater 'predictability'. The global pattern correlations between EOF1 and both $\delta\overline{[u]}_{\mathcal{C}}$ and the $\delta\overline{[u]}_{\mathcal{H}}$ yield *generally* high values in the small $\mathcal{C}$ - large $\mathcal{H}$ region, but are markedly low in the large $\mathcal{C}$ - small $\mathcal{H}$ region. In the former region, the model climate is characterized by a strong single jet, and EOF1 represents meander of the jet in the north-south direction. In the latter region, the time-mean zonal winds show a double jet structure, and EOF1 and EOF2 together represent quasi-periodic poleward propagation of zonal mean flow anomalies.

The above results indicate that climate predictability is (1) generally high if the dominant

form of internal variability represents zonal index, and (2) low if the dominant form of variability is characterized by poleward propagation. Since the climate response is stationary by definition, it is expected that the dominant form of internal variability must also be stationary. The zonal index satisfies this requirement, but the poleward propagation does not. In practice, however, both forms of internal variability can coexist in a single climate state. Our model calculations suggest the rule of thumb that the predictability is relatively high if the ratio of the fractional variance of EOF2 to that of EOF1, γ, does not exceed 0.5. Although not discussed by Taguchi (2003), the same general rule applies to his result. From the fractional variances displayed in Taguchi and Yoden (2002), we notice that for the 0- and 1000-m topography runs, for which the climate predictability was high, the values of γ are 0.14 and 0.45, respectively. In contrast, the value of γ for the 500-m topography case, which showed rather poor predictability, is 0.67.

Returning to our own result, there is, however, one exception to the above general rule. In the small $\mathcal{C}$ - large $\mathcal{H}$ corner where the zonal index is more prominent than elsewhere in the parameter space, we find that the global pattern correlations between EOF1 and $\delta\overline{[u]}_{\mathcal{H}}$ are not as high as suggested by γ. In other words, climate predictability tends to be higher with respect to changes in $\mathcal{C}$, than to changes in $\mathcal{H}$. An explanation for this behavior may be offered by considering the mechanism for driving the zonal index. Regardless of why the zonal index is the most prominent form of zonal flow variability[5], the zonal index basically arises

[5]There are explanations as to why the zonal index (north-south meander of the jet) dominates over jet pulsation (strengthening and weakening) in zonal flow variability. One explanation is that the extratropical baroclinic zone is broader than the meridional scale of the baroclinic eddies (Lee and Feldstein 1996; Vallis et al. 2004). The other is that the structure of the zonal index is more conducive to positive feedback from the eddy fluxes (Robinson 2000; Lorenz and Hartmann 2001). These two mechanisms, however, may not be

from fluctuations in the midlatitude baroclinic eddy vorticity flux (Robinson 1991; Yu and Hartmann 1993; Lee and Feldstein 1996; Feldstein and Lee 1998). Therefore, the stationary forcing ($\delta\mathcal{C}$ or $\delta\mathcal{H}$) causes a zonal-index-like change in the zonal mean flow only if the corresponding change in the eddy vorticity flux also take on a north-south dipole structure. Since the eddy vorticity flux ultimately arises from baroclinic instability, as $\delta\mathcal{C}$ increases, which causes a poleward expansion of the baroclinic zone, it seems reasonable to expect that the eddy vorticity flux will also extend into higher latitudes. Relative to a given reference climate state, this poleward shift of the eddy vorticity flux requires that the changes in the jet structure have a dipole form, with a positive (negative) sign on the jet's poleward (equatorward) side. This is indeed what we observe in Figs. 5a and 5b.

We next consider how $\delta\mathcal{H}$ may cause the same type of dipolar change in the eddy vorticity flux. According to the mechanism of Chang (1995), Robinson (2002), and Seager et al. (2003), a strengthening in the subtropical jet, caused by anomalous tropical heating, can shift the eddy vorticity flux equatorward. This equatorward shift implies that further changes in the jet take on a dipolar form, as before, but with positive (negative) sign on the jet's equatorward (poleward) side. Again, this behavior is observed throughout the entire $\mathcal{C}-\mathcal{H}$ parameter space (see Figs. 5c and 5d). On the other hand, SL shows that this equatorward shift in both the eddy fluxes and the jet is in part due to an equatorward expansion of the baroclinic zone, which in turn arises from the strengthened subtropical jet. Perhaps more

mutually exclusive. In the absence of a positive feedback, it may be that EOF1 would still have the largest amplitude among all the patterns at most times. As a result, the EOF1 pattern would have the greatest opportunity to develop a positive feedback with the eddies. This positive feedback could further amplify the pattern that is already most dominant.

importantly, because the changes in the jet structure arise from both anomalous diabatic heating and eddy vorticity fluxes, the extratropical zonal wind response to $\delta\mathcal{H}$ is more complicated than that for $\delta\mathcal{C}$. Therefore, one may expect that the resemblance of $\delta\overline{[u]}_{\mathcal{H}}$ to EOF1 will be less impressive than that for $\delta\overline{[u]}_{\mathcal{C}}$.

The finding that the climate predictability depends on the form of $[u]'$ variability also raises the question of what determines whether the variability takes the form of either the zonal index or the quasi-periodic poleward propagation. In a separate study, we find that the poleward propagation is caused by an orchestrated combination of equatorward radiation of Rossby waves, nonlinear breaking of these waves, and radiative relaxation. The latter two processes follow the first one, and as such the meridional radiation of Rossby waves is the central mechanism behind the poleward propagation (see also James and Dodd 1996). Since meridional radiation is prohibited if the potential vorticity (PV) gradient of the ambient flow is very sharp (Hoskins and Ambrizzi 1993; Swanson et al. 1997), one expects a relatively smooth PV gradient in the poleward propagation regime. This is indeed found to be the case. As a measure of the sharpness of the PV gradient, the meridional width of the 250-hPa quasi-geostrophic PV gradient, $\overline{[q]}_y$, is calculated, where the width is defined as the latitudinal distance over which the value of $\overline{[q]}_y$ is greater than 60% of its maximum value. The result, shown in Fig. 8, indicates that, compared with the zonal index regime (small $\mathcal{C}$ - large $\mathcal{H}$), $\overline{[q]}_y$ is systematically smooth and weak in the poleward propagation regime (large $\mathcal{C}$ - small $\mathcal{H}$). The smooth and weak $\overline{[q]}_y$, in turn, arises from the relatively low values of $\mathcal{H}$ which drive a subtropical jet of only moderate strength. This provides a physical explanation as to why the climate predictability is poor in the low $\mathcal{H}$ region.

6 Implication for climate predictability

This section considers implications of the model results for climate predictability, in particular for the Southern Hemisphere (SH) equinoctial states. As discussed in SL, the approximate parametric region for the SH equinoctial circulation is determined subjectively, and is indicated in Figs. 1a-c, 6, and 7 with the dashed oval. The identification of this parametric region (SH region, hereafter) for the SH flow is also suggested by the characteristics of the observed interannual variability in $[u]$. For any given year, the equinoctial mean $[u]$ in the SH may take the form of a double-jet, an intermediate-jet, or a single-jet. In addition, the intraseasonal variability of $[u]$ shows characteristics of both the poleward propagation (Riehl, 1951; Feldstein 1998) and the zonal index/ jet meander (Feldstein and Lee 1998; Hartmann and Lo 1998; Lorenz and Hartmann 2001). Although it is not shown, the value of χ in the SH equinoctial condition is around 0.25. Hartmann and Lo (1998) and Lorenz and Hartmann (2001) further point out that the value of γ in the SH is about 0.5. If only equinoctial states are examined, the value of γ turns out to be 0.47 (not shown). All of these observations justify the above choice for the SH region in the $\mathcal{C} - \mathcal{H}$ parameter space.

In the vicinity of the SH region, Fig. 6 indicates that the climate predictability of $\delta\overline{[u]}$ is overall reasonably good, but that the agreement between the EOF1 and $\delta\overline{[u]}_{\mathcal{C}}$ is much better in mid-latitudes (see Figs. 7b) than in low-latitudes (Fig. 7a). This result is consistent with the findings of Kushner et al. (2001). They find that the annular mode of their control climate is similar to the response of the SH mid-latitude circulation in their scenario climate. However, the same was not the case for their subtropical circulation. Based on the fact that the SH region is very close to the poleward propagation regime, we can also speculate that the

climate predictability of the SH is only marginally good. A slight shift toward the poleward propagation regime will considerably lower the climate predictability. It should be stated that these interpretations are yet tentative. The SH climate predictability is inferred from a set of simple PE model runs. Moreover, the model is incapable of simulating stratospheric processes which might be crucial for long-term forecast (e.g., Baldwin et al. 2003).

In this study, the perturbed heatings, $\mathcal{C}$ and $\mathcal{H}$, are highly idealized, and we do not use these parameters to mimic the real atmosphere or much more elaborate general circulation model simulations. As described in Son and Lee (2005), they are introduced to generate various climate states relevant for both the current and warmer/colder climates. Given the arbitrariness in the choice of these parameters, a similar set of calculations may be performed with different choice of parameters, or for the same parameters but with a different meridional and vertical structures in the radiative relaxation. However, we do not expect that such calculations would yield fundamentally different interpretations. For instance, a change in the structure of the heating and cooling will produce a different set of jets and their internal variability. As such, the 'SH climate' will occupy a different region in the new parameter space. Its location, however, will 'physically' be the same for that in this study: i.e., the boundary between single-jet and double-jet states, and between the zonal index and poleward propagation. Since the predictability along the regime boundary is relatively good, the predictability of the SH climate inferred from the new simulations will also be marginally good as in this study.

Acknowledgments

Comments from Dr. Steven Feldstein and Lindsey Williams are gratefully appreciated. This research was supported by the National Science Foundation through Grant No. ATM-0324908.

Appendix: Numerical model

Since the numerical simulations in this study are identical to those described in SL, we provide only a brief description of the numerical model.

The numerical model is a global spectral primitive equation (PE) model which is based on the dynamical core of the Geophysical Fluid Dynamics Laboratory general circulation model. In order to keep the computational time for the parameter study at a reasonable level, while resolving eddies with an acceptable accuracy, the model resolution is truncated at zonal wave number 15 (about 7.5° in longitude) and meridional wave number 30 (about 2.3° in latitude). In the vertical direction, 10 equally spaced sigma levels are used.

The above PE model is driven by relaxing the temperature field toward a radiative equilibrium profile, T_e, with a time scale τ_R of 30 days. In the experiments, the T_e profile is systematically varied by adding tropical heating and high-latitude cooling to base profile T_{base}:

$$T_e(\mathcal{C},\mathcal{H}) = T_{base} + \Delta T_e(\mathcal{C},\mathcal{H}), \tag{A.1}$$

with

$$\Delta T_e(\mathcal{C},\mathcal{H}) = \begin{cases} \underbrace{\mathcal{H}\cdot\alpha^{-1}\tau_R\sigma^{R/C_p}\cdot cos^2\left(\frac{\pi\varphi}{2\varphi_h}\right)}_{tropical\ heating} & \text{for} \quad 0^\circ \le \varphi \le \varphi_h \\ \underbrace{\mathcal{C}\cdot 2\alpha\tau_R\sigma^{R/C_p}\cdot\left\{cos\varphi_c(2cos\varphi - cos\varphi_c) - 1 + \frac{\alpha}{3}\right\}}_{high-latitude\ cooling} & \text{for} \quad \varphi_c \le \varphi \le 90^\circ \end{cases} \tag{A.2}$$

where α (= (1+2σ)/3) is a parameter which modulates both the meridional temperature gradient and the static stability. Two reference latitudes, φ_h (≡ 10°) and φ_c (≡ 45°), denote the poleward boundary of tropical heating and equatorward boundary of high-latitude

cooling, respectively. As stated in the introduction, $\mathcal{H}$ and $\mathcal{C}$ are, respectively, the surface heating and cooling rates (in units of Kday^{-1}) at the equator and the poles. All other notations are standard. Figure A1a shows the T_{base} profile, while Fig. A1b illustrates ΔT_e for ($\mathcal{C}$, $\mathcal{H}$) = (0.33, 0.33). The sum of these two fields, T_e (0.33, 0.33), is displayed in Fig. A1c.

References

Baldwin, M. P., D. B. Stephenson, D. W. J. Thompson, T. J. Dunkerton, A. J. Charlton, and A. O'Neill, 2003: Stratospheric memory and extended-range weather forecasts. *Science*, **301**, 636-640.

Chang, E. K. M., 1995: The influence of Hadley circulation intensity changes on extratropical climate in an idealized model *J. Atmos. Sci.*, **52**, 2006-2024.

Feldstein, S. B., 1998: An observational study of the intraseasonal poleward propagation of zonal mean flow anomalies. *J. Atmos. Sci.*, **55**, 2516-2529.

_____, and S. Lee, 1998: Is the Atmospheric Zonal Index Driven by an Eddy Feedback? *J. Atmos. Sci.*, **55**, 3077-3086.

Fyfe, J. C., G. J. Boer, and G. M. Flato, 1999: The Arctic and Antarctic Oscillations and their projected changes under global warming. *Geophys. Res. Lett.*, **26**, 1601-1604.

Hartmann, D. L., and F. Lo, 1998: Wave-driven zonal flow vacillation in the Southern Hemisphere. *J. Atmos. Sci.*, **55**, 1303-1315.

Hoskins, B. J., and T. Ambrizzi, 1993: Rossby wave propagation on a realistic longitudinally varying flow. *J. Atmos. Sci.*, **50**, 1661-1671.

James, I. N., and J. P. Dodd, 1996: A mechanism for the low frequency variability of the mid-latitude troposphere. *Quart. J. Roy. Meteor. Soc.*, **122**, 1197-1210.

James, P. M., K. Fraedrich, and I. N. James, 1994: Wave-zonal-flow interaction and ultra-low-frequency variability in a simplified global general circulation model. *Quart. J. Roy. Meteor. Soc.*, **120**, 1045-1067.

Kidson, J. W., 1988: Indices of the Southern Hemisphere zonal wind. *J. Climate*, **1**, 183-194.

Kushner, P. J., I. M. Held, and T. L. Delworth, 2001: Southern Hemisphere atmospheric circulation response to global warming. *J. Climate*, **14**, 2238-2249.

Lee, S., and S. Feldstein, 1996: Mechanism of zonal index evolution in a two-layer model. *J. Atmos. Sci.*, **53**, 2232-2246.

Lorenz, D. J., and D. L. Hartmann, 2001: Eddy-zonal flow feedback in the Southern Hemisphere. *J. Atmos. Sci.*, **58**, 3312-3327.

Namias, J., 1947: *Extended forecasting by mean circulation methods.* Washington, U. S. Department of Commerce, Weather Bureau, 89 pp.

Riehl, H., T. C. Yeh, and N. E. La seur, 1950: A study of variations of the general circulation. *J. Atmos. Sci.*, **7**, 181-194.

Robinson, W., 1991: The dynamics of the zonal index in a simple model of the atmosphere. *Tellus*, **43A**, 295-305.

_____, 2000: A baroclinic mechanism for the eddy feedback on the zonal index. *J. Atmos. Sci.*, **57**, 415-422.

_____, 2002: On the midlatitude thermal response to tropical warmth. *Geophys. Res. Lett.*, **29**, doi:10.1029/2001GL014158

Rogers, J. C., and H. van Loon, 1982: Spatial variability of sea level pressure and 500 mb height anomalies over the Southern Hemisphere. *Mon. Wea. Rev.*, **110**, 1375-1392.

Seager, R., N. Harnik, Y. Kushnir, W. Robinson, and J. Miller, 2003: Mechanisms of hemispherically symmetric climate variability. *J. Climate*, **16**, 2960-2978.

Son, S. -W., and S. Lee, 2005: The response of westerly jets to thermal driving in a primitive equation model. *J. Atmos. Sci.*, in press.

Swanson, K. L., P. J. Kushner, and I. M. Held, 1997: Dynamics of barotropic storm tracks. *J. Atmos. Sci.*, **54**, 791-810.

Taguchi, M., 2003: Tropospheric response to stratospheric degradation in a simple global circulation model. *J. Atmos. Sci.*, **60**, 1835-1846.

_____, and S. Yoden, 2002: A parameter-sweep experiment on the annular variability with a simple global circulation model. *J. Meteor. Soc. Japan*, **80**, 1077-1088.

Thompson, D. W. J., and J. M. Wallace, 1998: The Arctic Oscillation signature in the wintertime geopotential height and temperature fields. *Geophys. Res. Lett.*, **25**, 1297-1300.

_____, _____, and G. C. Hegerl, 2000: Annular modes in the extratropical circulation. Part II: Trends. *J. Climate*, **13**, 1018-1036.

Vallis, G. K., E. P. Gerber, P. J. Kushner, and B. A. Cash, 2004: A mechanism and simple dynamical model of the north Atlantic oscillation and annular modes. *J. Atmos. Sci.*, **61**, 264-280.

Weickmann, K. M., G. N. Kiladis, and P. D. Sardeshmukh, 1997: The dynamics of intraseasonal atmospheric angular momentum oscillations. *J. Atmos. Sci.*, **54**, 1445-1461.

Yu, J. -Y., and D. L. Hartmann, 1993: Zonal flow vacillation and eddy forcing in a simple GCM of the atmosphere. *J. Atmos. Sci.*, **50**, 3244-3259.

Figure caption

Figure 1. Summary of the parameter study as a function of $\mathcal{C}$ and $\mathcal{H}$. Values in parentheses along each axis are the vertically integrated diabatic heating and cooling rates at the equator and pole, respectively. (a) Jet structure: The intensity (in units of ms^{-1}) and latitudinal location of the jet are denoted inside and below each circle, respectively. The number of circles denotes the number of jets. Single- and double-jet regimes are cross hatched. (b) The parameter γ : the ratio of Var (EOF2) to Var (EOF1). The contour interval is 0.05 and values greater than or equal to 0.5 are shaded. The superimposed values are Var (EOF1). (c) The parameter χ : the maximum lag-correlation coefficients between PC1 and PC2. The contour interval is 0.05 and values greater than or equal to 0.5 are shaded. Numbers (in units of days) denoted in frame indicates lag days at which $\chi \geq 0.5$. (d) Summary of the 250-hPa-$[u]'$ variability.

Figure 2. One-point lag-correlation maps for the 250-hPa $[u]'$ with the base latitude at 30°, along the axis 'E' in Fig. 2a. The lag-correlations are calculated for each Hemisphere and then averaged. The contour interval is 0.1. Zero lines are omitted and positive values are shaded. The right side of each panel shows 250-hPa $\overline{[u]}$ with a thick gray line and EOF1 (EOF2) with a thin solid (dashed) line. The location of the polar front and subtropical jets are indicated by solid and dashed straight lines, respectively. The imposed values of ($\mathcal{C}$, $\mathcal{H}$) and Var (EOF_n) are denoted in each frame.

Figure 3. The left panels show time series of normalized PC1 (solid line) and PC2 (dashed line), for (a) ($\mathcal{C}$, $\mathcal{H}$) = (0.83, 0.33) Kday^{-1} and (b) ($\mathcal{C}$, $\mathcal{H}$) = (0.17, 1.67) Kday^{-1}. The right panels display the lag-correlation coefficients between the two PCs for the filtered (black)

and unfiltered (gray lines) data. These two experiments are highlighted in Fig. 1a with black circles.

Figure 4. The 250-hPa $\overline{[u]}$ for the positive phase (solid) and the negative phase (dashed) of EOF1 along the axis 'E' of Fig. 1a.

Figure 5. The top panels, from (a) to (d), are 250-hPa $\delta\overline{[u]}$ (contoured) and EOF1 (shaded), along the axes 'A', 'B', 'C', and 'D', shown in Fig. 1a, respectively. Both contour and shading intervals are 0.5 ms^{-1} for (a) and (b), and 1.0 ms^{-1} for (c) and (d). Dark (light) shading is for positive (negative) values. The bottom panels show the latitudinal location of the low-latitude (gray) and mid-latitude (black) maxima in 250-hPa $|\delta\overline{[u]}|$ (open) and $|EOF1|$ (filled squares). Examples of latitudinal distance between the two, $\delta\varphi$, are illustrated in (b). For these specific cases, the value of low- and mid-latitude $\delta\varphi_{\mathcal{C}}$ are 4° and 8°, respectively.

Figure 6. The pattern correlation between $\delta\overline{[u]}$ and EOF1. The contour interval is 0.05 and correlation coefficients greater than or equal to 0.8 are shaded.

Figure 7. The values of $\delta\varphi$ in the $\mathcal{C}-\mathcal{H}$ parameter space. Similar to the definitions for $\delta\overline{[u]}_{\mathcal{C}}$ and $\delta\overline{[u]}_{\mathcal{H}}$, $\delta\varphi_{\mathcal{C}}$ (upper panels) and $\delta\varphi_{\mathcal{H}}$ (lower panels) correspond to the $\delta\varphi$ that are parallel to the $\mathcal{C}$ and $\mathcal{H}$ axes, respectively. For each of these two measures, the low-latitude values are displayed on the left panel, and the mid-latitude values on the right panel. The contour interval is 1° and values less than or equal to 2°, which is approximately the model resolution, are shaded.

Figure 8. The meridional width of the 250-hPa $\overline{[q]}_y$. The contour interval is 2° and values greater than or equal to 35° are shaded. The superimposed values are the maximum $\overline{[q]}_y$ in

units of $10^{11}\mathrm{ms}^{-1}$.

Figure A1. (a) T_{base}, (b) heating profile for $(\mathcal{C}, \mathcal{H}) = (0.33, 0.33)$ Kday^{-1}, and (c) sum of (a) and (b). The contour intervals are 10K in (a) and (c), and 2K in (b). Zero lines are omitted.

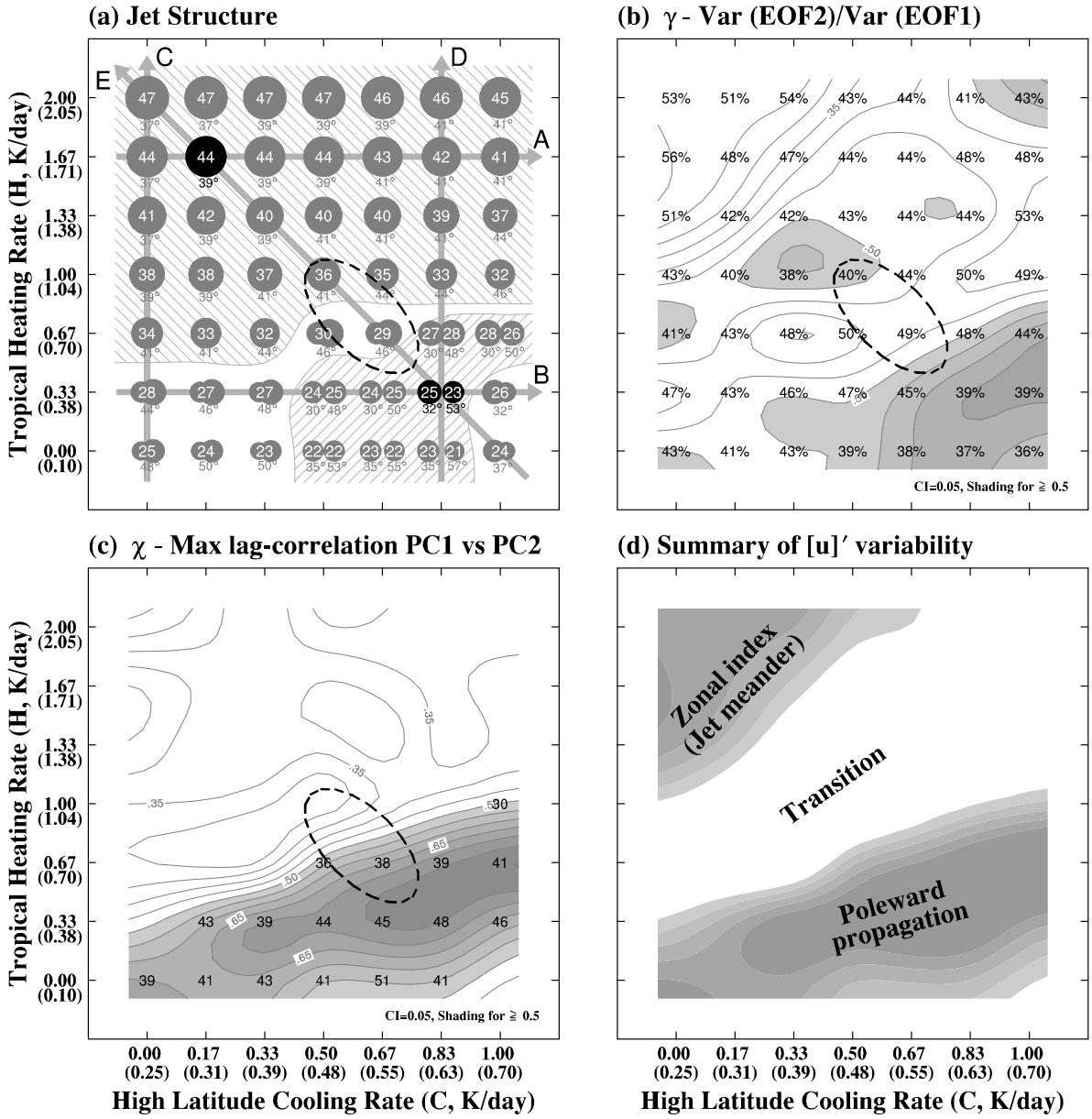

Figure 1: Summary of the parameter study as a function of $\mathcal{C}$ and $\mathcal{H}$. Values in parentheses along each axis are the vertically integrated diabatic heating and cooling rates at the equator and pole, respectively. (a) Jet structure: The intensity (in units of ms^{-1}) and latitudinal location of the jet are denoted inside and below each circle, respectively. The number of circles denotes the number of jets. Single- and double-jet regimes are cross hatched. (b) The parameter γ : the ratio of Var (EOF2) to Var (EOF1). The contour interval is 0.05 and values greater than or equal to 0.5 are shaded. The superimposed values are Var (EOF1). (c) The parameter χ : the maximum lag-correlation coefficients between PC1 and PC2. The contour interval is 0.05 and values greater than or equal to 0.5 are shaded. Numbers (in units of days) denoted in frame indicates lag days at which $\chi \geq 0.5$. (d) Summary of the 250-hPa-$[u]'$ variability.

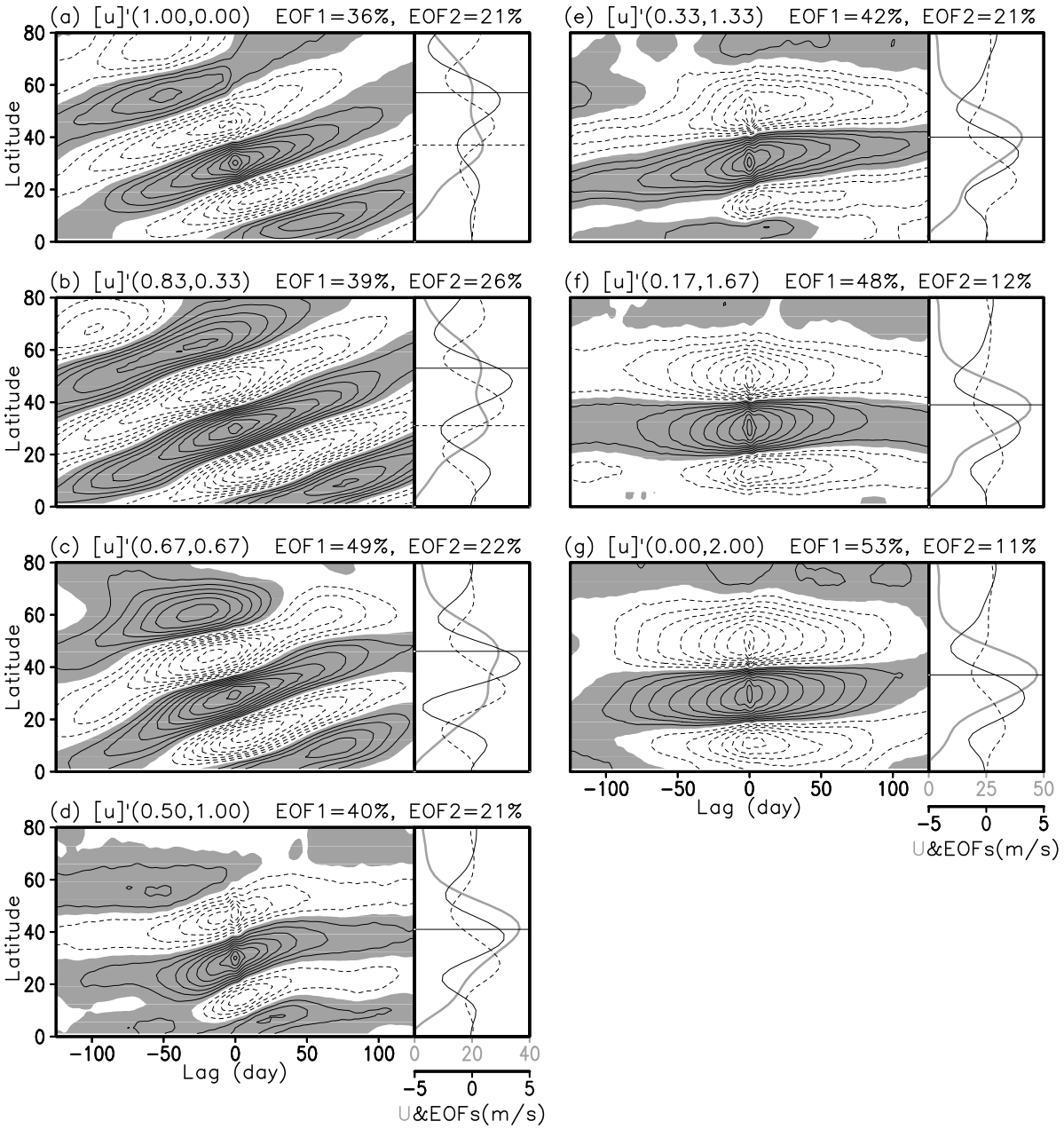

Figure 2: One-point lag-correlation maps for the 250-hPa $[u]'$ with the base latitude at 30°, along the axis 'E' in Fig. 2a. The lag-correlations are calculated for each Hemisphere and then averaged. The contour interval is 0.1. Zero lines are omitted and positive values are shaded. The right side of each panel shows 250-hPa $\overline{[u]}$ with a thick gray line and EOF1 (EOF2) with a thin solid (dashed) line. The location of the polar front and subtropical jets are indicated by solid and dashed straight lines, respectively. The imposed values of ($\mathcal{C}$, $\mathcal{H}$) and Var (EOF$_n$) are denoted in each frame.

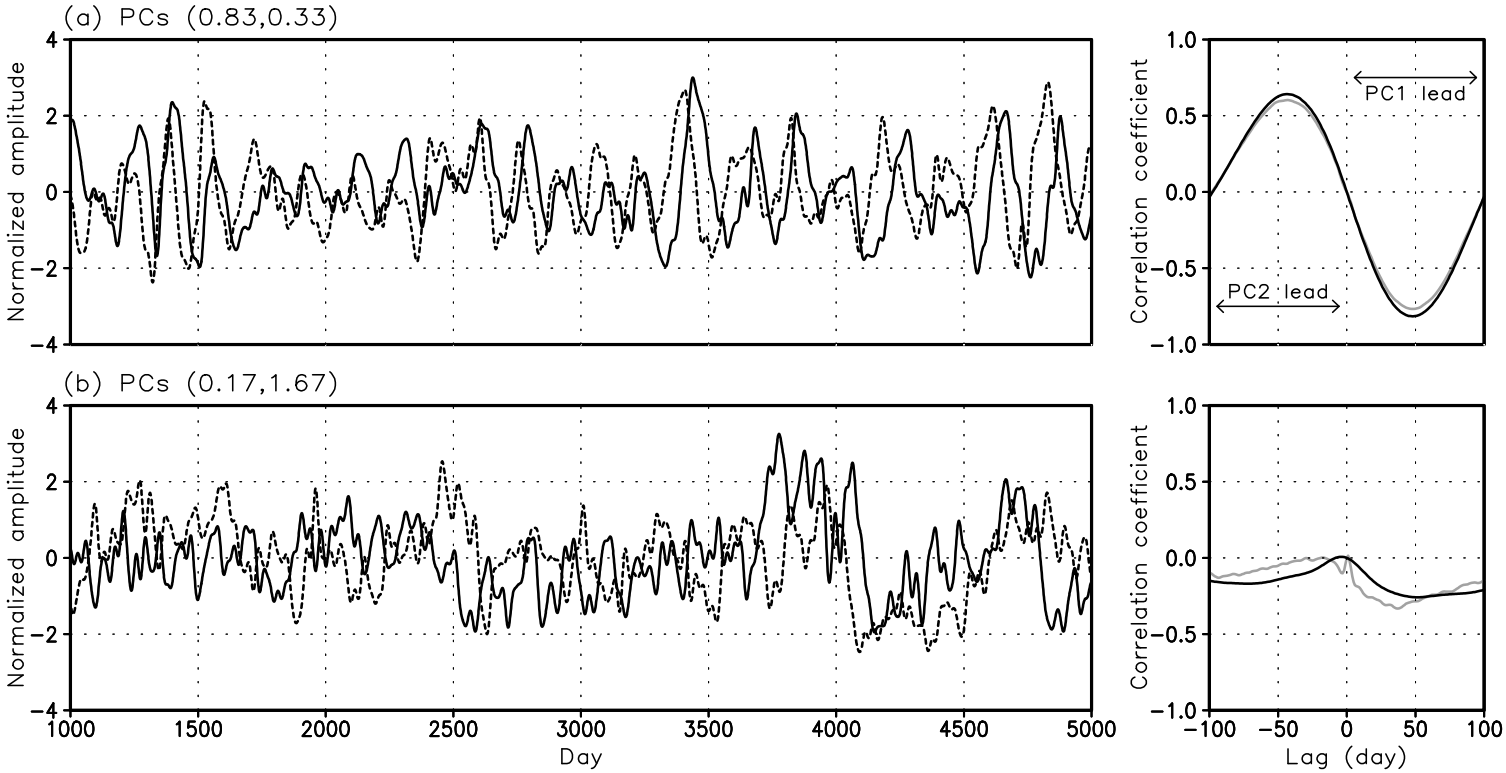

Figure 3: The left panels show time series of normalized PC1 (solid line) and PC2 (dashed line), for (a) $(\mathcal{C}, \mathcal{H}) = (0.83, 0.33)$ Kday^{-1} and (b) $(\mathcal{C}, \mathcal{H}) = (0.17, 1.67)$ Kday^{-1}. The right panels display the lag-correlation coefficients between the two PCs for the filtered (black) and unfiltered (gray lines) data. These two experiments are highlighted in Fig. 1a with black circles.

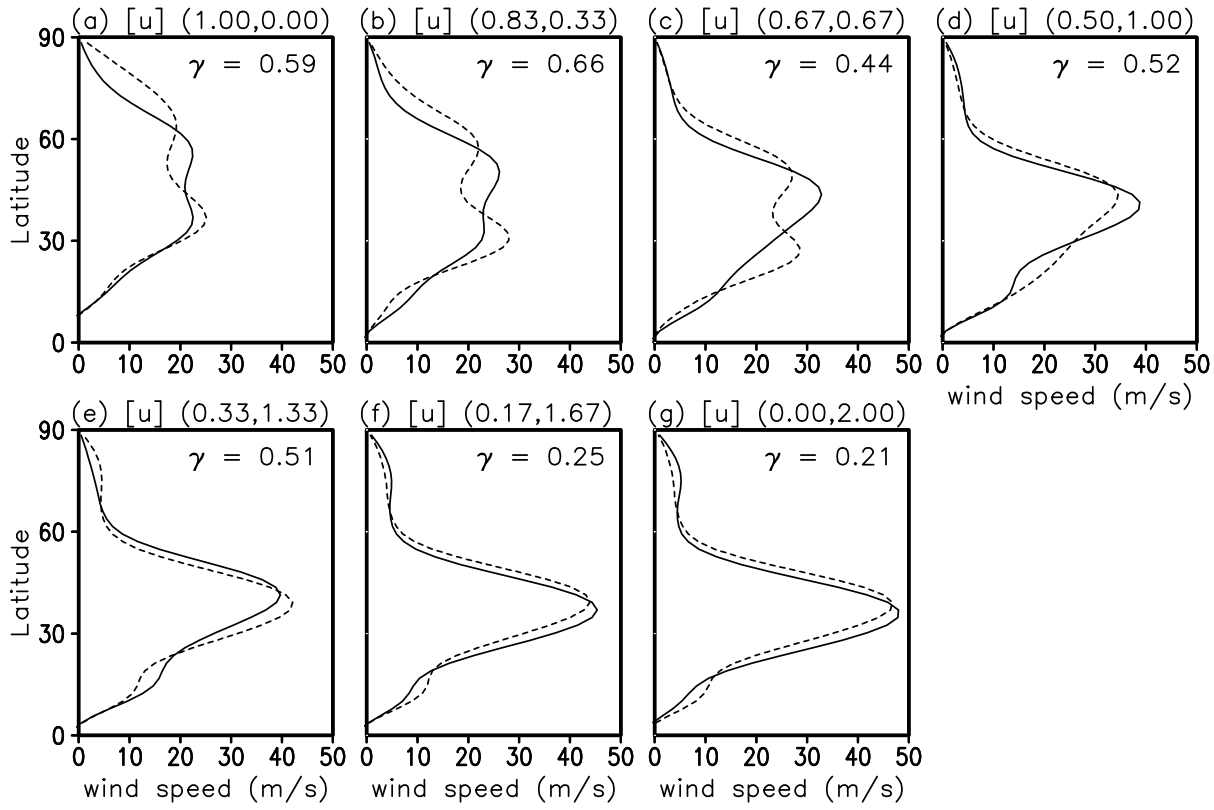

Figure 4: The 250-hPa $\overline{[u]}$ for the positive phase (solid) and the negative phase (dashed) of EOF1 along the axis 'E' of Fig. 1a.

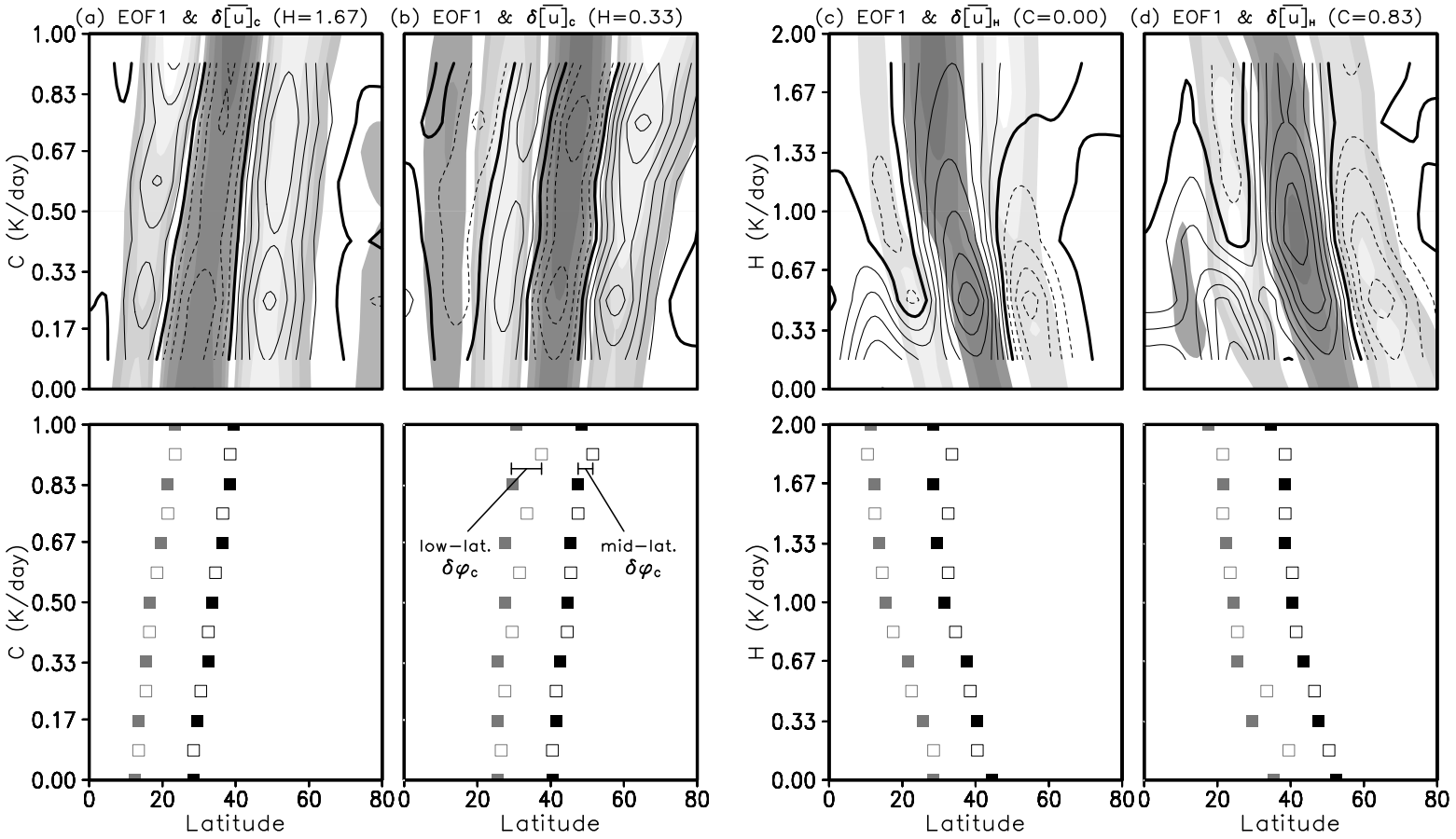

Figure 5: The top panels, from (a) to (d), are 250-hPa $\delta\overline{[u]}$ (contoured) and EOF1 (shaded), along the axes 'A', 'B', 'C', and 'D', shown in Fig. 1a, respectively. Both contour and shading intervals are 0.5 ms^{-1} for (a) and (b), and 1.0 ms^{-1} for (c) and (d). Dark (light) shading is for positive (negative) values. The bottom panels show the latitudinal location of the low-latitude (gray) and mid-latitude (black) maxima in 250-hPa $|\delta\overline{[u]}|$ (open) and $|EOF1|$ (filled squares). Examples of latitudinal distance between the two, $\delta\varphi$, are illustrated in (b). For these specific cases, the value of low- and mid-latitude $\delta\varphi_C$ are 4° and 8°, respectively.

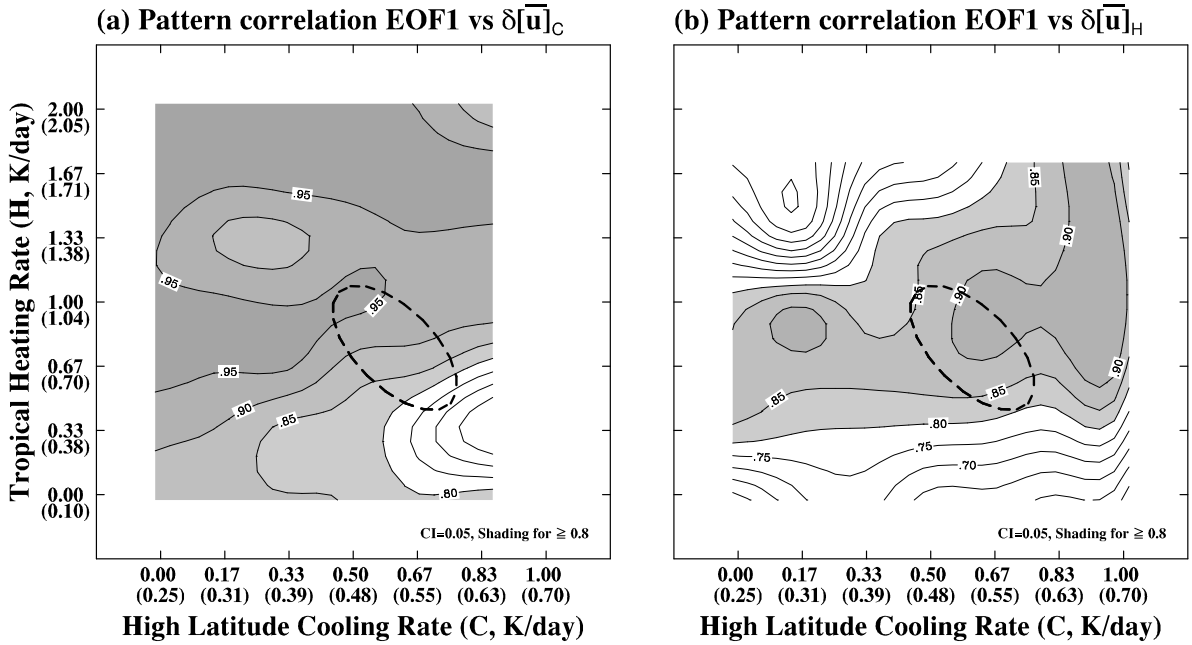

Figure 6: The pattern correlation between $\delta\overline{[u]}$ and EOF1. The contour interval is 0.05 and correlation coefficients greater than or equal to 0.8 are shaded.

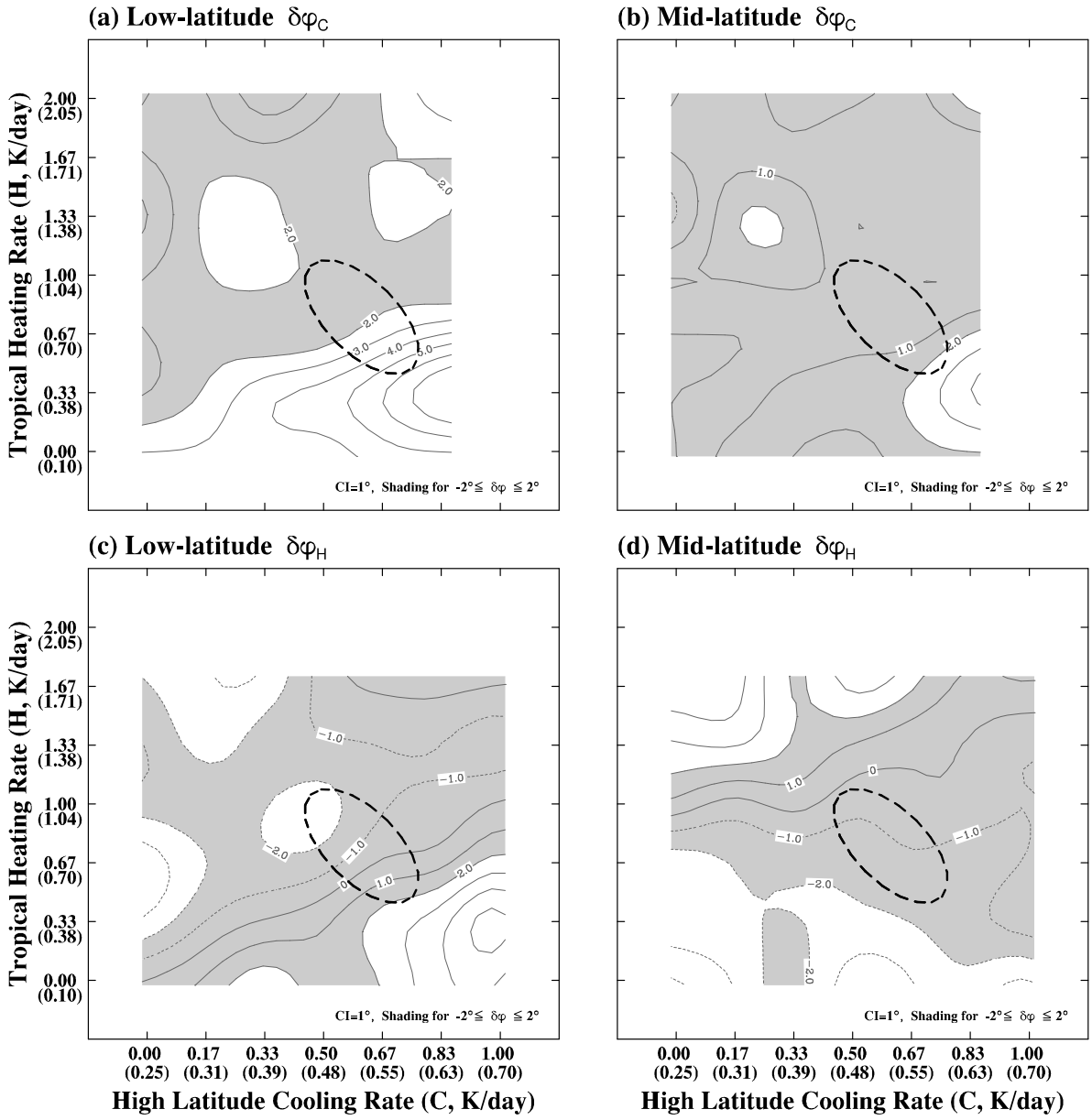

Figure 7: The values of $\delta\varphi$ in the $\mathcal{C} - \mathcal{H}$ parameter space. Similar to the definitions for $\delta\overline{[u]}_{\mathcal{C}}$ and $\delta\overline{[u]}_{\mathcal{H}}$, $\delta\varphi_{\mathcal{C}}$ (upper panels) and $\delta\varphi_{\mathcal{H}}$ (lower panels) correspond to the $\delta\varphi$ that are parallel to the $\mathcal{C}$ and $\mathcal{H}$ axes, respectively. For each of these two measures, the low-latitude values are displayed on the left panel, and the mid-latitude values on the right panel. The contour interval is 1° and values less than or equal to 2°, which is approximately the model resolution, are shaded.

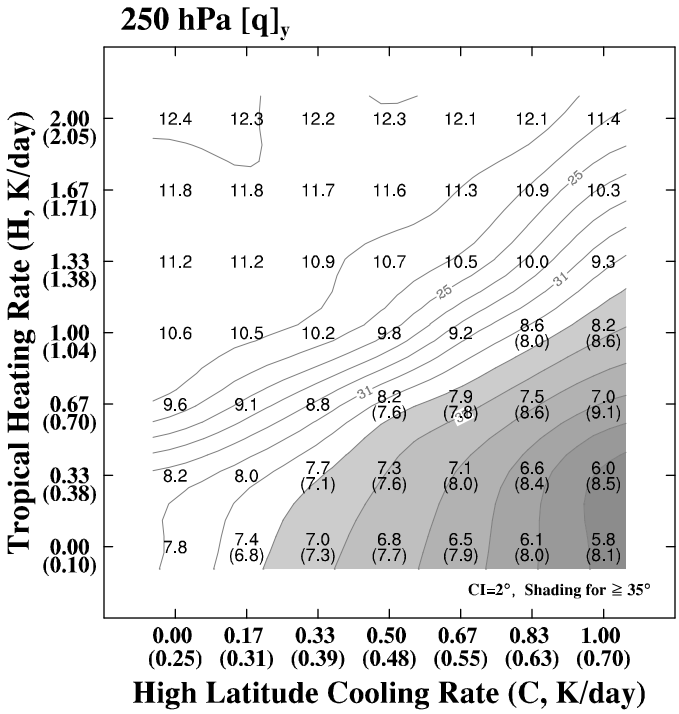

Figure 8: The meridional width of the 250-hPa $\overline{[q]}_y$. The contour interval is 2° and values greater than or equal to 35° are shaded. The superimposed values are the maximum $\overline{[q]}_y$ in units of $10^{11}\mathrm{ms}^{-1}$.

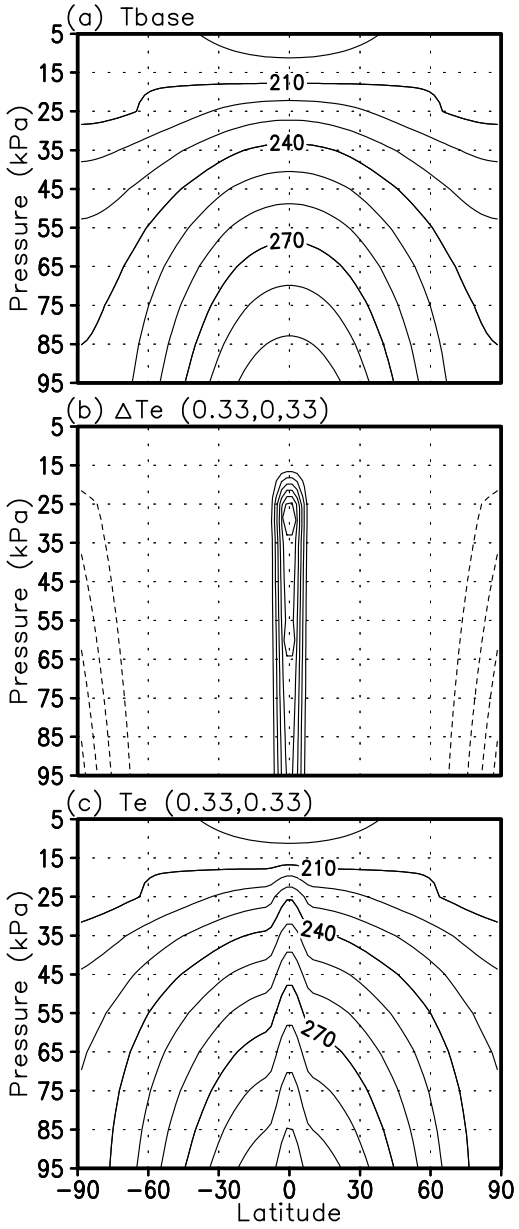

Figure A1: (a) T_{base}, (b) heating profile for ($\mathcal{C}$, $\mathcal{H}$) = (0.33, 0.33) Kday^{-1}, and (c) sum of (a) and (b). The contour intervals are 10K in (a) and (c), and 2K in (b). Zero lines are omitted.